The Astrophysical Journal Letters, 875:L20 (7pp), 2019 April 20 https://doi.org/10.3847/2041-8213/ab15dc

NuSTAR Measurement of Coronal Temperature in Two Luminous, High-redshift Quasars

G. Lanzuisi[1,2], R. Gilli[1], M. Cappi[1], M. Dadina[1], S. Bianchi[3], M. Brusa[1,2], G. Chartas[4], F. Civano[5], A. Comastri[1], A. Marinucci[3], R. Middei[3], E. Piconcelli[6], C. Vignali[1,2], W. N. Brandt[7,8,9], F. Tombesi[6,10,11,12], and M. Gaspari[13,14]
[1] INAF-Osservatorio di Astrofisica e Scienza dello Spazio di Bologna, via Gobetti 93/3, I-40129 Bologna, Italy; giorgio.lanzuisi@inaf.it
[2] Dipartimento di Fisica e Astronomia dell'Universitá degli Studi di Bologna, via P. Gobetti 93/2, I-40129 Bologna, Italy
[3] Dipartimento di Matematica e Fisica, Universitá degli Studi Roma Tre, via della Vasca Navale 84, I-00146 Roma, Italy
[4] Department of Physics and Astronomy of the College of Charleston, Charleston, SC 29424, USA
[5] Harvard-Smithsonian Center for Astrophysics, 60 Garden Street, Cambridge, MA 02138, USA
[6] INAF—Observatorio Astronomico di Roma, via Frascati 33, I-00040, Monte Porzio Catone, Roma, Italy
[7] Department of Astronomy and Astrophysics, 525 Davey Lab, The Pennsylvania State University, University Park, PA 16802, USA
[8] Institute for Gravitation and the Cosmos, The Pennsylvania State University, University Park, PA 16802, USA
[9] Department of Physics, 104 Davey Laboratory, The Pennsylvania State University, University Park, PA 16802, USA
[10] Department of Physics, University of Rome "Tor Vergata", Via della Ricerca Scientifica 1, I-00133 Rome, Italy
[11] Department of Astronomy, University of Maryland, College Park, MD 20742, USA
[12] NASA/Goddard Space Flight Center, Code 662, Greenbelt, MD 20771, USA
[13] Department of Astrophysical Sciences, Princeton University, 4 Ivy Lane, Princeton, NJ 08544-1001, USA
Received 2019 March 26; revised 2019 April 4; accepted 2019 April 4; published 2019 April 19

Abstract

X-ray emission from the active galactic nucleus (AGN) is believed to be produced via Comptonization of optical/ultraviolet seed photons emitted by the accretion disk, upscattered by hot electrons in a corona surrounding the black hole. A critical compactness versus temperature threshold is predicted above which any increase in the source luminosity, for a fixed size, would then generate positron–electron pairs rather than continue heating the coronal plasma. Current observations seem to confirm that all AGNs populate the region below this critical line. These models, however, have never been probed by observations in the high-luminosity regime, where the critical line is expected to reach low temperatures. To fill this observational gap, we selected two luminous ($\log(L_{\rm Bol}) > 47.5\,{\rm erg\,s^{-1}}$) quasars, 2MASSJ1614346+470420 ($z = 1.86$) and B1422+231 ($z = 3.62$), and obtained *XMM–Newton* and *NuSTAR* deep observations for them. We performed detailed spectral analysis of their quasisimultaneous soft and hard X-ray data, in order to constrain the parameters of their coronae. Using a phenomenological cutoff power-law model, with the inclusion of a reflection component, we derived rest-frame values of the high-energy cutoff of $E_{\rm cut} = 106^{+102}_{-37}$ keV and $E_{\rm cut} = 66^{+17}_{-12}$ keV, respectively. Comptonization models consistently give as best-fit parameters electron temperatures of ∼45 keV and ∼28 keV, respectively, and optically thick coronae ($\tau > 1$). These low coronal temperatures fall in the limited region allowed at these luminosities to avoid runaway pair production.

Key words: accretion, accretion disks – black hole physics – X-rays: galaxies

1. Introduction

The primary X-ray emission in active galactic nuclei (AGNs) is believed to be produced via Comptonization: optical/ultraviolet (UV) thermal photons emitted by the accretion disk are upscattered by electrons in a hot ($\sim 10^{8-9}$ K) corona surrounding the supermassive black hole (SMBH; Haardt & Maraschi 1993). The resulting spectrum can be described as a cutoff power law with a photon index and a high-energy cutoff (at energies around a few hundred keV) that depends on the electron temperature (kT_e) and the optical depth (τ) of the corona.

The characterization of the X-ray emission from AGN is therefore the best tool available to investigate the physical properties of the innermost regions around accreting SMBHs and to measure coronal properties such as temperature, optical depth, and geometry. Recent X-ray reverberation studies (De Marco et al. 2013; Reis & Miller 2013; Cackett et al. 2014; Kara et al. 2016) suggest that the size R_c of the hot corona producing the X-rays is in the range ∼3–20 R_g, where $R_g = GM/c^2$ is the gravitational radius for a black hole of mass M. Such a range has also been independently confirmed via microlensing studies (e.g., Pooley et al. 2007; MacLeod et al. 2015; Chartas et al. 2016).

Since interactions between high-energy photons in compact systems produce electron–positron pairs, it was soon realized that pair production in AGN coronae may act as an effective thermostat (e.g., Svensson 1984; Stern et al. 1995). In fact, any rise in electron temperature T_e or compactness $\ell \propto L/R$ (Cavaliere & Morrison 1980)[15] above a critical curve in the temperature-compactness plane, the so-called "pair line," would result in a runaway pair production, causing the temperature to drop.

Early studies were based on high-energy X-ray missions such as *CGRO*, *BeppoSAX*, *Integral*, *Swift*-BAT, and Suzaku, mounting nonimaging instruments whose ability to obtain high signal-to-noise ratio (S/N) spectra and measure spectral cutoffs were limited to bright nearby sources ($F_x > 10^{-11}\,{\rm erg\,s^{-1}\,cm^{-2}}$). Yet, they showed that local Seyfert galaxies exhibit coronae with a broad range of temperatures ($E_{\rm cut} = 50$–500 keV, Perola et al. 2002; Dadina 2008;

[14] *Spitzer* Fellow.

[15] The dimensionless compactness ℓ is defined as the luminosity L over the size R of the emitting region, $\ell = L\sigma_T/Rm_ec^3$.

Vasudevan et al. 2013; Malizia et al. 2014) in the luminosity range $L_X = 10^{42}$–10^{44} erg s^{-1}.

NuSTAR (Harrison et al. 2013) is now providing a major advance in the understanding of AGN coronae. Its bandwidth is limited to ∼80 keV, but its sensitivity is orders of magnitude better than previous missions, allowing accurate measurements of the cutoff in local AGN. Fabian et al. (2015, F15 hereafter) compiled a list of all high-energy cutoffs measured by *NuSTAR* and investigated the ℓ versus T_e relation in detail. The temperature was derived assuming $E_{cut}/kT_e \sim 2$ as found by Comptonization models for optically thin coronae (e.g., Petrucci et al. 2001) and R_c was generally assumed to be $10R_g$. Most sources were found to be below the ℓ versus T_e critical line defining the region forbidden by the onset of pair production.

In general it is difficult to tightly constrain cutoff values exceeding the observed bandpass (Parker et al. 2015) except for sources with very high photon statistics (see, e.g., García et al. 2015; Matt et al. 2015). *NuSTAR* measurements, all performed so far in nearby ($z < 0.06$) low luminosity log $L_X < 45$ erg s^{-1} AGN, are in fact limited by the *NuSTAR* bandpass ($E_{cut} < 200$ keV).

Therefore the high-L_X, high-E_{cut} regime has never actually been probed. However, thanks to its greater sensitivity, *NuSTAR* is now capable of testing runaway pair-production models by measuring coronal properties in high-redshift, high-luminosity quasars where larger E_{cut} values can be constrained thanks to the cosmological redshifting of the cutoff downward in observed-frame energy.

We present here the first firm measurement of E_{cut} in two high-redshift ($z \gtrsim 2$), high-luminosity ($L_{Bol} > 47$ erg s^{-1}) quasars. This Letter is organized as follows: Section 2 describes the target selection, and Section 3 describes the data reduction. In Section 4 we report the different spectral models adopted, and in Section 5 we summarize our results. We adopt the cosmological parameters $H_0 = 70$ km s^{-1} Mpc^{-1}, $\Omega_\Lambda = 0.73$, and $\Omega_m = 0.27$. Errors are given at the 90% confidence level.

2. Target Selection and Observations

In order to select luminous quasars, bright enough in the X-ray band to allow for a good characterization of the high-energy cutoff, we considered all known quasars with $F_{0.5\text{–}10keV} > 5 \times 10^{-13}$ erg s^{-1} cm^{-2} at spectroscopic redshift $z_{spec} > 1.5$, both lensed and nonlensed sources.

Lensed AGNs were selected from the CASTLES catalog.[16] The brightest lensed source in this catalog is B1422+231 (hereafter B1422). The lensing factor is estimated to be ∼20 (Assef et al. 2011).

As for nonlensed sources, we searched for the brightest quasars by cross-correlating the X-ray point-source catalogs from *Chandra*, *XMM–Newton*, and *ROSAT* (CSC v2, 3XMM-DR6, and RASS-BSC), with the 12th SDSS-III data release. The brightest one is 2MASSJ1614346+470420 (hereafter 2MASSJ16). These two sources (B1422 and 2MASSJ16) were observed quasisimultaneously with *XMM–Newton* and *NuSTAR* in 2017 as part of a *NuSTAR* Cycle 3 program (P.I.: G. Lanzuisi).[17] Their properties are summarized in Table 1.

We note that B1422 is classified as moderately radio-loud ($R = 90$, Dadina et al. 2016) with a steep radio continuum ($\alpha_r = 0.9$, Orienti et al. 2007), indicating that the source is highly inclined in the plane of the sky. In this case, the radio emission should be dominated by the lobes, and not by the jet, and the X-ray spectrum is not strongly contaminated by the jet component (see the discussion in Dadina et al. 2016).

3. Data Reduction

B1422 was observed by *XMM–Newton* on 2017 December 29 for 38 ks and by *NuSTAR* on 2017 December 30 for 101 ks. 2MASSJ16 was observed by *XMM–Newton* on 2017 August 5 for 98 ks, and followed up by *NuSTAR* on 2017 August 28 and 2017 October 9 for 106 and 48 ks, respectively.

For both sources, *XMM–Newton* EPIC data were reduced using the standard software `SAS` v.16.1.[18] A filter for periods of high background rate was adopted using a threshold of 0.5 and 0.2 counts per seconds in the 10–12 keV band, for pn and MOS, respectively. We selected only events corresponding to single and double pixel events (pattern 0–4 and 0–12 for pn and MOS respectively). The source spectra were extracted from circular regions of 40″ radius, corresponding to ∼90% encircled energy fraction. The background spectra were extracted from an area ∼10 times larger than the source region, surrounding the quasar. The final exposure times were 25ks pn (35ks MOS) for B1422 and 69ks pn (84ks MOS) for 2MASSJ16.

The *NuSTAR* data were processed using the *NuSTAR* Data Analysis Software package (NuSTARDAS) v.1.8.0 within `Heasoft` v.6.20 tools.[19] Calibrated and cleaned event files were produced using the calibration files in the *NuSTAR* CALDB (version 20170727) and standard filtering criteria with the `Nupipeline` task. We checked for high background period using the `nustar_filter_lightcurve` IDL script.[20] The two *NuSTAR* observations for 2MASSJ16 were taken at 40 days of distance, and we verified that no significant variability was detected before merging the two data sets with standard `Heasoft` tools. The final, cleaned *NuSTAR* exposure times are 85ks for B1422 and 140 ks for 2MASSJ16.

In order to reduce the background and increase the spectral S/N at high energies, we tested different extraction regions, and finally adopted a region of 40″ radius, corresponding to ∼60% of the encircled energy fraction for the *NuSTAR* point-spread function (An et al. 2014). This allowed us to detect the source at $>3\sigma$ in the 20–50 keV band in both sources and to better sample the high-energy range.

4. Spectral Modeling

The final spectra have 1.2×10^4 and 3.0×10^4 total, 0.3–10 keV *XMM–Newton* counts and 1800 and 2300 total, 3–50 keV *NuSTAR* counts for B1422 an 2MASSJ16, respectively. The spectral modeling is performed with the package `Xspec` v.12.9.1, using the the C-stat statistic (Cash 1979), and binning the spectra to five counts per bin, because *NuSTAR* spectra are in the low-counts regime. Given the quality of the available data we choose not to include in our analysis complex models such as relativistic reflection. All the models described below are modified by a Galactic column density of

[16] See https://www.cfa.harvard.edu/castles.

[17] B1422 has also been observed with *Chandra* several times, for a total of 125 ks, the most recent one being in 2012. In order to avoid long-term variability issues (see, e.g., Lanzuisi et al. 2016) we focus our analysis on the coeval *XMM–Newton* and *NuSTAR* data.

[18] https://www.cosmos.esa.int/web/xmm-newton/sas

[19] https://heasarc.nasa.gov/lheasoft/

[20] https://github.com/NuSTAR/nustar-idl

Table 1
Target Properties

Target	z_{spec}	μ	L_{Bol} (erg s^{-1})	logM_{BH} ($M_\odot$)	Edd.	*XMM–Newton* (ks)	*NuSTAR* (ks)
(1)	(2)	(3)	(4)	(5)	(6)	(7)	(8)
B1422	3.62	20[a]	47.15[a]	9.7[a]	0.21	25	85
2MASSJ16	1.86	⋯	47.79[b]	9.8[b]	0.71	69	140

Notes. (1) Target name, (2) redshift, (3) lensing factor, (4) log. of the bolometric luminosity, (5) log. of the SMBH mass in $M_\odot$, (6) Eddington ratio, defined as L_{Bol}/L_{Edd}, (7) *XMM–Newton*-pn cleaned exposure time, and (8) *NuSTAR* cleaned exposure time.
[a] Assef et al. (2011), L_{Bol} derived from the delensed $L_{1450Å}$ (20% conservative error estimate); M_{BH} from H$_\beta$.
[b] Shen et al. (2011), M_{BH} from Mg II.

$N_H = 3.2 \times 10^{20}$ cm^{-2} for B1422 and 0.9×10^{20} cm^{-2} for 2MASSJ16, respectively (Kalberla et al. 2005).

4.1. Phenomenological Model

As a first step we fitted the *XMM–Newton* and *NuSTAR* spectra for both sources with a phenomenological model: a power law with an exponential high-energy cutoff and Compton reflection from cold material in a slab geometry, including emission lines (model `Pexmon` in `Xspec`, Nandra et al. 2007). The intensity of the reflection is parameterized with R, defined as the solid angle covered by the cold, reflecting material, as visible from the Comptonizing source, in units of 2π.

Given the possible degeneracy between spectral slope, intensity of the reflection, and high-energy cutoff (Perola et al. 2002), all these component must be fitted simultaneously. The free parameters of the model are, therefore, the power-law photon index Γ; the high-energy cutoff E_{cut}; the reflection parameter R; and the continuum normalization. In both sources, intrinsic cold absorption in addition to the Galactic value is not required.

The model is the same for all four data sets (pn, MOS1 +MOS2,[21] and *NuSTAR* FPMA and FPMB) and a flux cross-calibration C_i is applied between the different instruments with values always smaller than 1.15 (the spectral slopes Γ obtained fitting each instrument separately are consistent within errors). We fixed all element abundances to solar values and fixed the inclination angle to $i = 60°$. We tested that adopting a different inclination angle has a limited impact on the resulting E_{cut} (few % difference for $i = 30°$ and $i = 80°$), while it has a strong impact on the reflection parameter: R is a factor $\sim$2 lower (higher) for $i = 30°$ ($i = 80°$).

As can be seen from Figure 1 (top left and right), the phenomenological model is able to fully reproduce the broadband spectrum of both quasars, and the *NuSTAR* data are crucial to constrain the high-energy cutoff of the continuum. The best-fit continuum parameters are summarized in Table 2.

Performing the fit with the `Pexrav` model (Magdziarz & Zdziarski 1995) plus the Fe Kα emission line, we get consistent best-fit results for the continuum parameters. In addition, in B1422 the line is detected at 90% c.l., with parameters $E_{line} = 6.50^{+0.18}_{-0.14}$ keV and EW $= 80^{+60}_{-40}$ eV rest frame (consistent with the results obtained in Dadina et al. (2016) from a deeper *XMM–Newton* observation), while in 2MASSJ16 it is marginally detected, with EW < 125 eV.

[21] MOS1 and 2 spectra merged, and response matrices averaged with standard HEASARC `ftools`, http://heasarc.gsfc.nasa.gov/ftools/.

Confidence contours for Γ and R versus E_{cut} are shown in Figure 1 (lower panels). All three continuum parameters are well constrained. The photon index is typical of quasars (Piconcelli et al. 2005), while the reflection parameter is higher than the one measured by *NuSTAR* in luminous quasars (Del Moro et al. 2017; Zappacosta et al. 2018): at $L_X > 10^{45}$ erg s^{-1} the typical reflection parameter is $R < 1$.

Finally, the E_{cut} values are lower than the average observed for low-luminosity AGNs: $E_{cut} = 66^{+17}_{-12}$ keV and $E_{cut} = 106^{+102}_{-37}$ keV for B1422 and 2MASSJ16, respectively, implying coronal temperatures of $\sim$33 keV and $\sim$53 keV, assuming $E_{cut}/kT_e \sim 2$ for optically thin coronae (Petrucci et al. 2001). For B1422, our best-fit E_{cut} is consistent, within 1σ, with the results from Dadina et al. (2016), but the uncertainties derived here are 50% smaller.

These E_{cut} values place the two quasars in the narrow region allowed by the runaway pair-production models: in Figure 2 (left) we translated the ℓ versus T_e plane from F15 in terms of directly observable quantities, i.e., L_X versus E_{cut}. The critical L_X versus E_{cut} lines are obtained from the theoretical critical ℓ versus T_e lines of Stern et al. (1995) for the two assumed coronal geometries, i.e., a slab or a hemisphere above the accretion disk. In the conversion we assumed $R_c = 10\,R_g$ and $M_{BH} = 10^8\,M_\odot$ (the mean mass of the F15 sample, thick lines) and $M_{BH} = 10^9\,M_\odot$ (as appropriate for luminous and massive quasars, dashed lines).

We updated the *NuSTAR* compilation of F15 by adding six more AGNs with measured E_{cut} from recent literature (Kammoun et al. 2017; Tortosa et al. 2017; Buisson et al. 2018; Younes et al. 2019). We also updated, for nine sources, the values of E_{cut} obtained in Malizia et al. (2014) with Integral, with the ones derived with *NuSTAR* in Molina et al. (2019). The new E_{cut} values are in very good agreement with the previous ones, with narrower error bars. Finally, we added the results from Ricci et al. (2018) from a large sample of local AGNs observed with *Swift*-BAT, binned in compactness. Again we used $R_c = 10\,R_g$ and $M_{BH} = 10^8\,M_\odot$ to convert from physical to observable quantities.

Most sources in Figure 2 (left) lie where the runaway pair-production model predicts. Some are close to the critical lines (NGC 5506 being the highest *NuSTAR*-constrained E_{cut}), but always below the theoretical limits for pair balance, suggesting that pair-production acts to regulate the coronal temperature. The two quasars analyzed here strikingly fall in the restricted region of high luminosity–low temperature allowed by the model.

Finally, we note that the observed E_{cut} should be corrected for the effect of gravitational redshift. This can be parameterized with the g-factor $g = E^i_{cut}/E^o_{cut}$. Tamborra et al. (2018a)

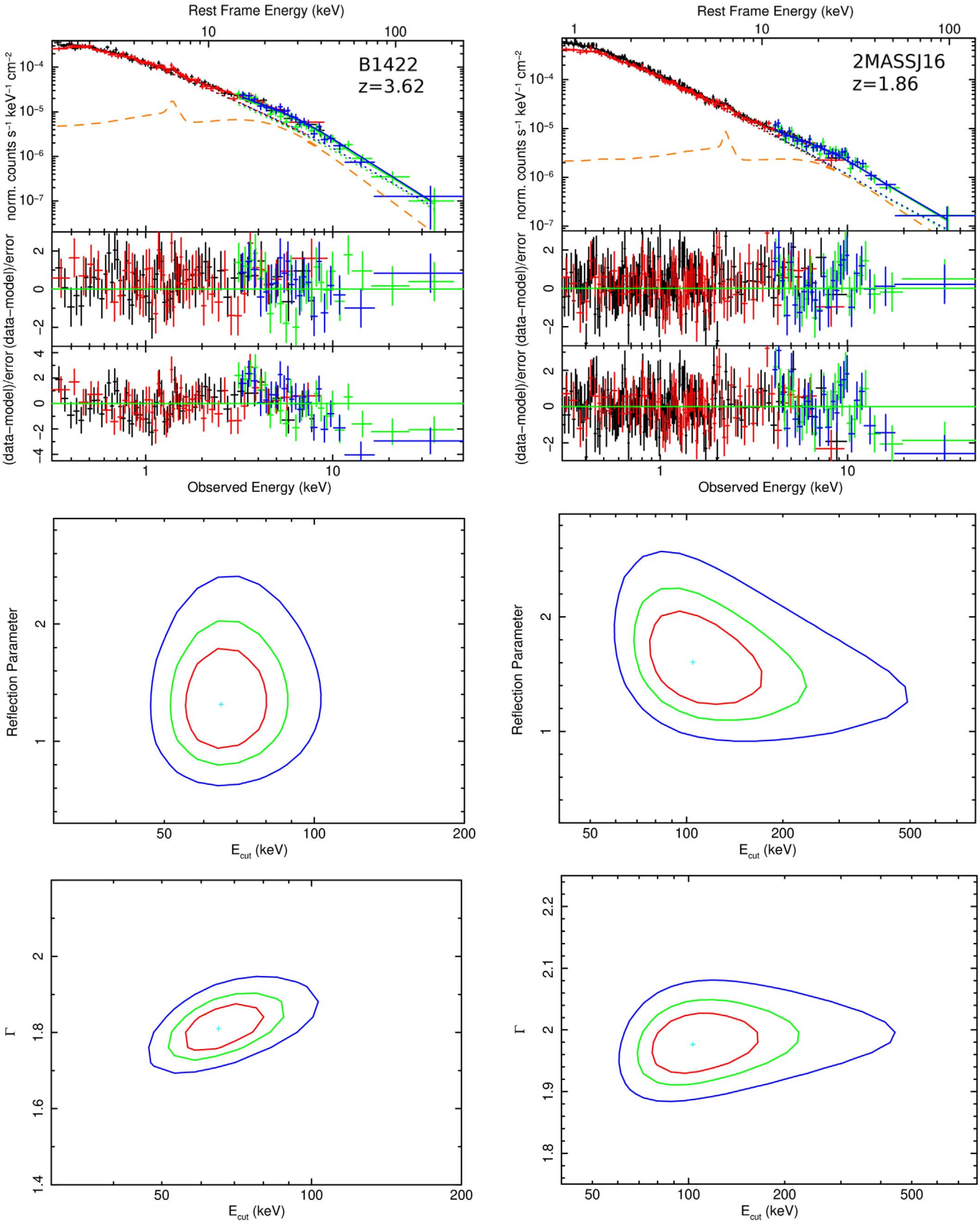

Figure 1. Top: normalized spectra and residuals from the fit of B1422 (left) and 2MASSJ16 (right) with the phenomenological model. The lower panels show residuals from the fit with no high-energy cutoff. Black, red, green, and blue points show *XMM–Newton* pn, MOS1+2, *NuSTAR* FPMA and FPMB data, respectively. Data binned for plotting purposes. The orange dashed lines show the reflection component. Center: confidence contours, at 68%, 90%, and 99% c.l., of the reflection parameter R vs. $E_{\rm cut}$. Bottom: same for the photon index Γ vs. $E_{\rm cut}$.

Table 2
Best-fit Parameter Values for the `pexmon` Model

Target	Γ	$E_{\rm cut}$ keV	R	$F_{0.5-10}$ (10^{-13} cgs)	$\log L_{2-10}$ (erg s^{-1})	$C_{\rm MOS}$	$C_{\rm FPMA}/C_{\rm FPMB}$	$Cstat/d.o.f.$
(1)	(2)	(3)	(4)	(5)	(6)	(7)	(8)	(9)
B1422	$1.81^{+0.07}_{-0.06}$	66^{+17}_{-12}	$1.3^{+0.5}_{-0.4}$	9.5	45.30	1.03	1.02/1.11	1637/1668
2MASSJ16	$1.98^{+0.11}_{-0.05}$	106^{+102}_{-37}	$1.6^{+0.7}_{-0.5}$	6.7	45.97	0.94	1.09/1.12	1705/1735

Note. (1) Target name, (2) photon index, (3) high-energy cutoff in keV, (4) reflection parameter, (5) Observed *XMM–Newton* 0.5–10 keV flux in erg s^{-1} cm^{-2}, (6) log. of the intrinsic (delensed) 2–10 keV luminosity in erg s^{-1}, (7) *XMM–Newton* MOS cross-calibration with respect to pn, (8) *NuSTAR* FPMA/FPMB cross-calibration with respect to pn, and (9) *Cstat/d.o.f* of the best fit.

computed how g depends on the radius/height of the corona, its emissivity profile, the BH spin, and the system inclination. For $R_c = 10$ and most combinations of these parameters, g falls between 1 and 1.18, being at most 1.38 for a maximally spinning BH seen at 30° with steep radial emissivity profile (r^{-3}). The redshifting of relativistic reflection may also contribute to the shift of $E^o_{\rm cut}$ to a lesser extent.

4.2. Comptonization Model

We tested also the physical, Comptonization model `NthComp` in Xspec (Życki et al. 1999). In order to properly take into account also the nonnegligible reflection component derived with the phenomenological model, we used the `xillverCp` reflection model (García et al. 2014) that uses `NthComp` as primary emission and self-consistently compute reflection from a nonrelativistic medium. The free parameters are the electron temperature kT_e, the photon index Γ, the ionization parameter of the reflector, and the reflection fraction. The optical depth τ can be derived indirectly from kT_e and Γ (Zdziarski et al. 1996).

The best-fit model, with comparable $Cstat/d.o.f.$ of the phenomenological model, has very low electron temperatures of $kT_e = 22^{+7}_{-2}$ keV for B1422 and $kT_e = 42^{+10}_{-11}$ keV for 2MASSJ16, and optical depths significantly above unity, $\tau = 3.6^{+0.6}_{-0.4}$ and $\tau = 2.0^{+0.3}_{-0.2}$, respectively. The ionization parameter of the reflector is consistent with 0, and the reflection parameter is similar to the one derived with the phenomenological model ($R = 1.4$–1.8).

We further tested these results using the Monte Carlo Comptonization model MoCA (Tamborra et al. 2018b, Marinucci et al. 2018). The kT_e and τ obtained with MoCA, and derived from the photon index and $E_{\rm cut}$ results from the phenomenological model, are $kT_e = 26^{+8}_{-3}$ keV and $\tau = 3.2^{+0.6}_{-0.8}$ for B1422, and $kT_e = 44^{+26}_{-11}$ keV and $\tau = 1.6^{+0.8}_{-0.7}$ for 2MASSJ16 in the slab geometry. The spherical geometry gives marginally higher optical depths ($\tau = 5.4^{+0.8}_{-1.4}$ and $\tau = 2.6^{+1.4}_{-1.2}$, respectively) for consistent electron temperatures.

Both physical models agree in finding low coronal temperatures, around $kT_e = 25$–45 keV, and optical depth substantially above unity, $\tau = 1.5$–3.5. This implies that the appropriate conversion factor between the observed high-energy cutoff and the electron temperature should be $E_{\rm cut}/kT_e \sim 3$ instead of 2 for these sources (Petrucci et al. 2001).

4.3. Absorption Model

For B1422 two possible solutions were explored in Dadina et al. (2016): the reflection and the complex-absorption scenarios. They were both consistent with the *XMM–Newton* data available at that time, from a statistical point of view. Therefore, we also tested a model in which a complex absorber covers the primary cutoff power law (`zxipcf×cutoffpl` in Xspec) for both of our quasars. When fitted to the *XMM–Newton* data alone, we obtained in both cases a reasonably good fit with the following parameters: covering factor $f_c \sim 0.3$–0.4, absorber column density $N_{\rm H} \sim (0.5$–$0.7) \times 10^{24}$ cm^{-2}, and low ionization ($\log\xi \sim 1.5$ erg cm s^{-1}). With the addition of *NuSTAR* data, however, it is clear that the reflection model is to be preferred (see also Risaliti et al. 2013 results on NGC 1365), because we measure large $\Delta Cstat$ between the two best-fit models: $\Delta C = 24$ for B1422 and 15 for 2MASSJ16, for two more free parameter.

Interestingly, in the complex-absorption scenario, only lower limits can be derived for the high-energy cutoff: $E_{\rm cut} > 235$ keV 2MASSJ16 and $E_{\rm cut} > 171$ keV for B1422, at 90% c.l. These values, coupled with a higher intrinsic luminosity, by a factor of 1.4–1.6, implied by the absorption model, would move both sources within the forbidden region in the l–T_e plane, in tension with the pair-production scenario.

Therefore, an incorrect modeling of the continuum, still consistent with the data below 10 keV for both quasars, would suggest wrong conclusions about the position of these two quasars in the pair-production runaway forbidden region, while the addition of *NuSTAR* data clearly rules out this possibility.

5. Conclusions

The $E_{\rm cut}$ values measured in this work for two luminous, high-redshift quasars, fall in the restricted region of the luminosity–temperature plane allowed by runaway pair production at such high luminosities. Our results on these sources expand by almost one order of magnitude the luminosity range sampled by hard X-ray $E_{\rm cut}$ measurement. The values of $E_{\rm cut}$ derived here are the first ones well determined for luminous quasars based on *NuSTAR* and *XMM–Newton* quasisimultaneous data. Consistent results with larger error bars were obtained for B1422 in Dadina et al. (2016) based on *XMM–Newton* data alone, but the lack of hard X-ray data made the results model-dependent (see Section 4.3). A tentative $E_{\rm cut}$ measurement of $E_{\rm cut} = 160^{+450}_{-80}$ keV was presented in Lanzuisi et al. (2016) for PG 1247 + 267, a hyper-luminous ($L_{\rm Bol} = 10^{48}$ erg s^{-1}) z = 2 quasar, but the nonsimultaneity of the soft and hard X-ray data again left the possibility of different interpretations of the combined spectra, giving degenerate results.

Recent results from the *Swift*-BAT sample (Ricci et al. 2018) show that the average $E_{\rm cut}$ of the sample anticorrelates with the Eddington ratio. At the $\lambda_{\rm Edd}$ ratio levels of B1422 and 2MASSJ16, $\lambda_{\rm Edd} = 0.2$ and 0.7, respectively (see Table 1), the

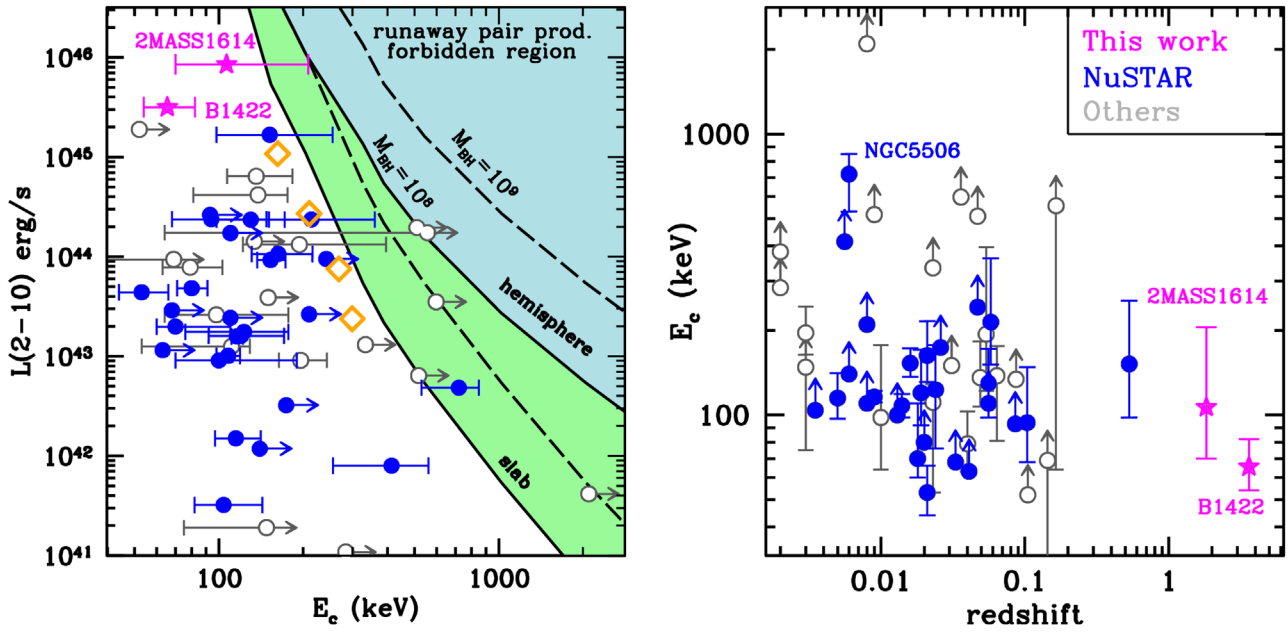

Figure 2. Left: E_{cut} vs. L_X for the updated F15 sample (*NuSTAR* measurements in blue, nonfocusing hard X-ray telescopes in gray). The two quasars analyzed here are in magenta. The cyan (green) area shows the forbidden region due to runaway pair-production for an hemispheric (slab) corona for $M_{BH} = 10^8\,M_\odot$. Dashed lines show the same limits for $M_{BH} = 10^9\,M_\odot$. Orange diamonds show the results from the BAT AGN survey (Ricci et al. 2018). Right: E_{cut} vs. redshift for the same samples reported in the left panel.

average values for the *Swift*-BAT sample are $E_{cut} \sim 190$ and $\sim$170 keV. The E_{cut} measured for the two quasars is therefore lower than for local sources accreting at the same Eddington rate. The main difference is the luminosity range, because $\log(L_x/\mathrm{erg\,s^{-1}}) > 45$ is not covered by the *Swift*-BAT sample.

Our results show that *NuSTAR* has effectively opened a new observational window, allowing for the first time measurement of coronal temperatures in AGN beyond $z = 1$ (Figure 2, right), where the redshift effect allows, in principle, measurement of E_{cut} values as high as a few hundred keV in bright quasars. Future observations of other high-redshift, luminous sources will expand the sample of E_{cut} measured in this regime and further test the validity of the pair-production model. To substantially increase the sample over which to test the pair-production forbidden region, larger effective area in the hard band (as proposed for HEX-P; see R. Hickox et al. 2019, in preparation) is needed to collect enough counts for accurate spectral analysis of faint sources.

We thank the anonymous referee for very valuable comments. This work is based on observations obtained with the *NuSTAR* mission, a project led by Caltech, managed by JPL, and funded by NASA; *XMM–Newton*, an ESA science mission funded by ESA and NASA. This research has made use of tools from NASA's HEASARC, a service of Goddard SFC and the SAO. G.L., M.C., and S.B. acknowledge financial support from the Italian Space Agency under grant ASI-INAF I/037/12/0, and n. 2017-14-H.O. F.T. acknowledges support by the "Rita Levi Montalcini" 2014 program. M.G. is supported by the Lyman Spitzer Jr. Fellowship (Princeton University) and by NASA *Chandra* GO7-18121X.

ORCID iDs

G. Lanzuisi https://orcid.org/0000-0001-9094-0984
R. Gilli https://orcid.org/0000-0001-8121-6177
S. Bianchi https://orcid.org/0000-0002-4622-4240
M. Brusa https://orcid.org/0000-0002-5059-6848
G. Chartas https://orcid.org/0000-0003-1697-6596
C. Vignali https://orcid.org/0000-0002-8853-9611
W. N. Brandt https://orcid.org/0000-0002-0167-2453
F. Tombesi https://orcid.org/0000-0002-6562-8654
M. Gaspari https://orcid.org/0000-0003-2754-9258

References

An, H., Madsen, K. K., Westergaard, N. J., et al. 2014, Proc. SPIE, 9144, 91441Q
Assef, R. J., Denney, K. D., Kochanek, C. S., et al. 2011, ApJ, 742, 93
Buisson, D. J. K., Fabian, A. C., & Lohfink, A. M. 2018, MNRAS, 481, 4419
Cackett, E. M., Zoghbi, A., Reynolds, C., et al. 2014, MNRAS, 438, 2980
Cash, W. 1979, ApJ, 228, 939
Cavaliere, A., & Morrison, P. 1980, ApJL, 238, L63
Chartas, G., Rhea, C., Kochanek, C., et al. 2016, AN, 337, 356
Dadina, M. 2008, A&A, 485, 417
Dadina, M., Vignali, C., Cappi, M., et al. 2016, A&A, 592, A104
De Marco, B., Ponti, G., Cappi, M., et al. 2013, MNRAS, 431, 2441
Del Moro, A., Alexander, D. M., Aird, J. A., et al. 2017, ApJ, 849, 57
Fabian, A. C., Lohfink, A., Kara, E., et al. 2015, MNRAS, 451, 4375
García, J., Dauser, T., Lohfink, A., et al. 2014, ApJ, 782, 76
García, J. A., Steiner, J. F., McClintock, J. E., et al. 2015, ApJ, 813, 84
Haardt, F., & Maraschi, L. 1993, ApJ, 413, 507
Harrison, F. A., Craig, W. W., Christensen, F. E., et al. 2013, ApJ, 770, 103
Kalberla, P. M. W., Burton, W. B., Hartmann, D., et al. 2005, A&A, 440, 775
Kammoun, E. S., Risaliti, G., Stern, D., et al. 2017, MNRAS, 465, 1665
Kara, E., Alston, W. N., Fabian, A. C., et al. 2016, MNRAS, 462, 511
Lanzuisi, G., Perna, M., Comastri, A., et al. 2016, A&A, 590, A77
MacLeod, C. L., Morgan, C. W., Mosquera, A., et al. 2015, ApJ, 806, 258
Magdziarz, P., & Zdziarski, A. A. 1995, MNRAS, 273, 837
Malizia, A., Molina, M., Bassani, L., et al. 2014, ApJ, 782, L25
Marinucci, A., Bianchi, S., Braito, V., et al. 2018, MNRAS, 478, 5638
Matt, G., Baloković, M., Marinucci, A., et al. 2015, MNRAS, 447, 3029
Molina, M., Malizia, A., Bassani, L., et al. 2019, MNRAS, 484, 2735
Nandra, K., O'Neill, P. M., George, I. M., et al. 2007, MNRAS, 382, 194
Orienti, M., Dallacasa, D., & Stanghellini, C. 2007, A&A, 475, 813
Parker, M. L., Tomsick, J. A., Miller, J. M., et al. 2015, ApJ, 808, 9
Perola, G. C., Matt, G., Cappi, M., et al. 2002, A&A, 389, 802
Petrucci, P. O., Haardt, F., Maraschi, L., et al. 2001, ApJ, 556, 716
Piconcelli, E., Jimenez-Bailón, E., Guainazzi, M., et al. 2005, A&A, 432, 15

Pooley, D., Blackburne, J. A., Rappaport, S., et al. 2007, ApJ, 661, 19
Reis, R. C., & Miller, J. M. 2013, ApJL, 769, L7
Ricci, C., Ho, L. C., Fabian, A. C., et al. 2018, MNRAS, 480, 1819
Risaliti, G., Harrison, F. A., Madsen, K. K., et al. 2013, Natur, 494, 449
Shen, Y., Richards, G. T., Strauss, M. A., et al. 2011, ApJS, 194, 45
Stern, B. E., Poutanen, J., Svensson, R., et al. 1995, ApJL, 449, L13
Svensson, R. 1984, MNRAS, 209, 175
Tamborra, F., Matt, G., Bianchi, S., & Dovčiak, M. 2018b, A&A, 619, A105
Tamborra, F., Papadakis, I., Dovčiak, M., & Svoboda, J. 2018a, MNRAS, 475, 2045
Tortosa, A., Marinucci, A., Matt, G., et al. 2017, MNRAS, 466, 4193
Vasudevan, R. V., Brandt, W. N., Mushotzky, R. F., et al. 2013, ApJ, 763, 111
Younes, G., Ptak, A., Ho, L. C., et al. 2019, ApJ, 870, 73
Zappacosta, L., Comastri, A., Civano, F., et al. 2018, ApJ, 854, 33
Zdziarski, A. A., Johnson, W. N., & Magdziarz, P. 1996, MNRAS, 283, 193
Życki, P. T., Done, C., & Smith, D. A. 1999, MNRAS, 309, 561